UAV Icing: Icing Effects on Control Surfaces

Markus Lindner* and Richard Hann†
Norwegian University of Science and Technology, Trondheim, Norway
UBIQ Aerospace, Trondheim, Norway

In-flight icing has a negative impact on the aerodynamic performance of fixed-wing, uncrewed aerial vehicles (UAVs). This paper investigates numerically, using ANSYS Fluent, the effect of leading-edge ice accretion on the aerodynamics of the control surface. To achieve that, 2D computational fluid dynamics (CFD) simulations of a wing with three different experimentally generated ice shapes are conducted. The ice shapes represent glaze, mixed, and rime ice. The ice shapes were accreted for 20 minutes and represent a flight through a CFR 14 Part 25 Appendix C continuous maximum cloud. The influence of ice shapes on the lift and pitching moment coefficients is investigated for five control surface deflections: −5°, 0°, 5°, 10°, and 15°. Furthermore, the influence on stall speed and longitudinal control derivatives $C_{L_{\delta_e}}$ and $C_{m_{\delta_e}}$ is evaluated. The airfoil used is an RG-15 with a chord length of 0.3 m. The flight velocity is 25 m/s. The results show that all ice shapes result in a reduction in lift and stall angle. Deflections of the control surface on the iced wing increase the lift, however, significantly less compared to the same clean case. The effect on the pitching moment shows a tendency to decrease longitudinal stability flight characteristics. Moreover, when deflecting the control surfaces, a nose-down moment is created. The stall speed increases, leading to additional drag due to the higher velocity and the higher drag coefficient of the accreted ice. The longitudinal control derivatives $C_{L_{\delta_e}}$ and $C_{m_{\delta_e}}$ show reduced control surface effectiveness due to leading-edge ice accretion. However, a dependency of the control derivatives on the flight velocity could not be found. The findings of this study extend the understanding of in-flight icing beyond its known effects on lift and drag, highlighting its influence on the control surfaces. These results can be integrated into rigid-body aerodynamic simulations to analyze the flight dynamics of UAVs experiencing leading-edge ice accretion.

I. Introduction

In-flight icing, also known as in-cloud icing, poses a significant vulnerability to the safe operation of uncrewed fixed-wing aerial vehicles (UAVs), also known as unmanned aerial vehicles, remotely piloted aircraft systems (RPAS), drones, or uncrewed aerial systems (UAS) [1].

In-flight icing occurs when an aircraft, UAV, or any kind of object maneuvers through a cloud with supercooled liquid droplets or encounters supercooled large droplets in freezing rain and freezing drizzle conditions [2, 3]. Supercooled liquid droplets are water droplets inside a cloud whose temperature is below their freezing point but are still in liquid form. A UAV flying through an icing cloud will have impingement of supercooled liquid droplets on all exposed surfaces. Mainly depending on the temperature, velocity, and the amount of water in the air, also known as liquid water content (LWC), the droplets will freeze on impact or run along the surface and freeze eventually. The ratio between the water that freezes on the surface and runs back is called the freezing fraction and indicates the type of ice prevailing [4, 5].

When encountering icing conditions, a UAV unprotected against ice accretion can experience severe aerodynamic penalties, leading to reduced operational times, mission aborts, and even the loss of the entire UAV [1, 6, 7]. Ice can accrete on any exposed surface, such as antennas, fairings, and the pitot tube, but has the most severe impact on the wings and propeller [8]. While ice accretion on the propeller leads to reduced thrust and increased torque, the wing experiences reduced lift, increased drag, and additional weight due to the ice mass [9–11]. The ice on the leading-edge of the wing disturbs the airflow around the airfoil and, depending on the shape of the ice, can lead to an ice-induced separation bubble that, depending on the angle of attack (AOA) and the ice shape, eventually reattaches [12–14]. The change in the flow field results in a significant change in the C_m curve, leading to negative static stability. In cases of

*Ph.D. Student, Department of Engineering Cybernetics, Norwegian University of Science and Technology (NTNU), e-Mail: markus.lindner@ntnu.no

†Senior-Researcher, Department of Engineering Cybernetics, Norwegian University of Science and Technology (NTNU), e-Mail: richard.hann@ntnu.no

high AOA, the airflow does not reattach to the airfoil. If this separation occurs in front of the location where control surfaces such as ailerons or flaps are located downstream, this affects their effectiveness and can lead to a loss of control of the aircraft [15].

This paper investigates numerically the impact of leading-edge ice on the controllability of a fixed-wing UAV with a wing-span of a few meters and about 25 kg maximum take-off weight. The emphasis will be on the influence of different ice shapes on the aerodynamics of an airfoil with deflected control surfaces, specifically their effects on lift, drag, moment, and separation. Furthermore, it examines the effectiveness of different control surface deflections with leading-edge ice. This work extends the work done previously by Högnadottir et al. in [16].

To understand the flight characteristics of an iced UAV, it is not sufficient to implement the degradation of lift, drag, and pitching moment. In order to develop a rigid body aerodynamic simulator, the effects of leading-edge ice accretion on the longitudinal control derivatives $C_{L_{\delta e}}$ and $C_{m_{\delta e}}$ have to be taken into account. In the context of this paper, δ_e represents any control surface deflection.

An experimental investigation on the effects of ice on aircraft stability and control was conducted by Ranaudo et al. in [17]. Using the DH-6 icing research aircraft and artificial horizontal tail ice, they were able to determine longitudinal stability and control derivatives for different flap configurations and measure changes in the longitudinal stability and control derivatives.

Baars et al. published a review paper, summarizing icing effects on an aircraft's aeroelastic stability [18]. Two frequently detected icing effects on stability and control were studied in more detail: elevator limit cycle oscillations with loss of elevator control effectiveness, and unstable dutch roll events.

The results of this paper expand the knowledge of ice accretion on the leading-edge for small fixed-wing UAVs to its effects on the control surface downstream. This helps to understand the impact of in-flight icing in addition to its adverse effects on lift and drag. The values presented can be used in a rigid body aerodynamic simulator to study the flight behaviour of an iced UAV by extending the knowledge about control derivatives for iced configurations. This paper discusses the need for ice protection systems in the context of manoeuvrability and controllability. The particular vulnerability of these control surfaces to disturbed airflow is demonstrated to UAV developers.

II. Methods

A. Investigated Cases

In this study, 2D computational fluid dynamics (CFD) simulations are performed for different control surface deflections and ice shapes. The airfoil used is an RG-15 airfoil that is widely applied for UAV applications. The chord length is 0.3 m, the flight velocity is 25 m/s, representing a typical chord length and velocity for a UAV of this category. The icing duration is set to 20 min, suggesting the approximate duration of a flight through a CFR 14 Part 25 Appendix C continuous maximum icing cloud [2].

The study investigates three experimentally created ice shapes, accumulated at three different temperatures. The temperatures are –2 °C, –4 °C, and –10 °C, representing glaze, mixed, and rime ice, respectively. The ice shapes have been created in the icing wind tunnel of VTT in Helsinki, Finland [19]. An icing wind tunnel provides a controlled environment for the accumulation of ice shapes by setting the temperature and the LWC. The spray system of the wind tunnel at VTT produces droplets with a median volumetric diameter (MVD) of 27.2 µm and a known droplet size distribution. The LWC for these experiments was chosen to be 0.52 g/m^3. The angle of attack during the ice accretion process was set to 4° to ensure realistic flight operations. To digitize the experimental ice shapes, the structure-from-motion technology photogrammetry was used. To transform the 3D ice shape into 2D, maximum combined cross-sections (MCCSs) have been created. More details on the preparation of the experimental ice shapes can be found in [20]. In addition to that, the ice shapes used can also be found there.

To demonstrate the influence of leading-edge ice on the control surface, five deflection angles are investigated: −5°, 0°, 5°, 10°, and 15°. A positive deflection angle indicates a downwards deflection of the control surface, generating a negative, pitch-down moment. Each deflection is simulated under clean, i.e., un-iced conditions, and with the above-mentioned three ice shapes, resulting in a total of 20 cases. This paper investigates an isolated airfoil. Depending on the UAV configuration, the UAV can be a flying wing with no possibility of counteracting additional moments, or it can have a horizontal stabilizer to counter unintended pitching [21]. To implement the control surface on the regular RG-15 airfoil, XFOIL was used [22]. The control surface starts at 70% of the chord length. The hinge point is set in the middle of the airfoil.

Furthermore, the influence of leading-edge ice accretion on the control surface effectiveness is evaluated for the four ice types, and its dependency on the velocity is studied. For this velocity study, additional simulations are conducted at velocities of 15 m/s, 20 m/s, 25 m/s, and 30 m/s.

B. Simulation Setup

The simulation of the flow field and performance parameters is performed using ANSYS Fluent Release 2025 R1 [23, 24]. An AOA sweep is performed from -2° to 15° with an increment of 1°. In the range close to the stall angle, the resolution is increased to 0.5° increments. To ensure better comparability between the different cases, all performance simulations are conducted at 0 °C. The flow simulations of the clean cases are calculated with a laminar-turbulent transition of the flow. The iced cases are expected to be fully turbulent immediately due to the ice roughness. Both types of simulations use the k-ω-SST turbulence model. To account for the ice roughness, the iced area is assigned a sand-grain roughness. The roughness height of the different ice types is calculated according to [25] and shown in Table 2. The formula presented there is not validated for low Reynolds number applications. However, the equivalent roughness height is expected to be a secondary effect on performance degradation, as simulations are run in fully turbulent conditions. A brief study on the influence of roughness height and transition or fully turbulent on performance degradation can be found in Appendix A. The clean cases are calculated with no roughness. The most significant simulation settings are summarized in Table 1.

Table 1 Simulation settings

Airfoil type	RG-15
Chord length	0.3 m
Air speed	25 m/s
Reynolds Number	560,000
Angles of Attack	$-2°$ ... 15°
Turbulence model, clean cases	k-ω-SST, transitional
Turbulence model, iced cases	k-ω-SST, fully turbulent
Static air pressure p	101325 Pa

Table 2 Equivalent sand-grain roughness height

Ice Type	Roughness Height
Rime	0.2238 mm
Mixed	0.2096 mm
Glaze	0.1667 mm

C. Grid Setup

The computational grid has been created using the commercial software Pointwise 2023.2.2 [26]. Since Fluent requires volume cells to compute, a 2D grid has been extruded by one cell in the spanwise direction . The grid was created as a hybrid O-grid with structured elements near the wing to ensure a boundary layer resolution. The first cell height at the wing surface has been selected to satisfy the dimensionless first cell height Y+ < 1 criteria. The growth rate of cells of the boundary layer resolution is 1.13.

The grid boundaries have the shape of an isosceles trapezoid, where the two legs and the shorter base represent the inlet, and the longer base represents the outlet. The opening angle of the trapezoid is chosen to accommodate the whole AOA range. The grid extends in both directions, upstream and downstream of the wing, to 40 times its chord length. To illustrate the grid, a schematic layout is depicted in Fig. 1 with the wing size not to scale. The number of cells of the clean wing grids is about 240,000, and for cases with leading-edge ice, about 245,000. Examples of a clean and an iced grid are depicted in Fig. 2 and 3.

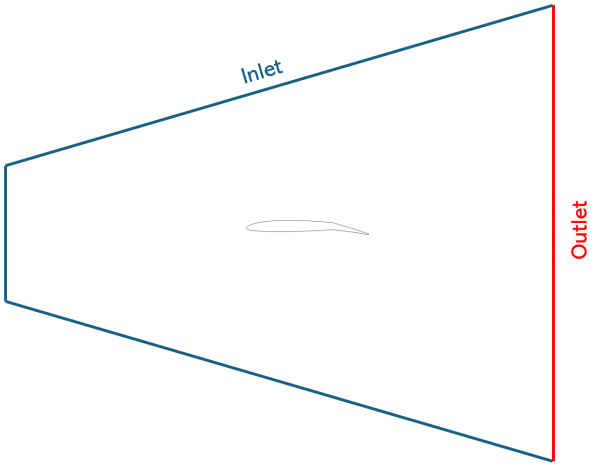

Fig. 1 Schematic layout of the calculation domain.

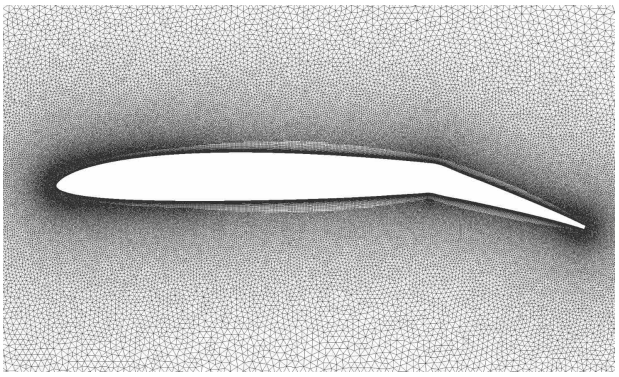

Fig. 2 Simulation grid with control surface deflection of 15°.

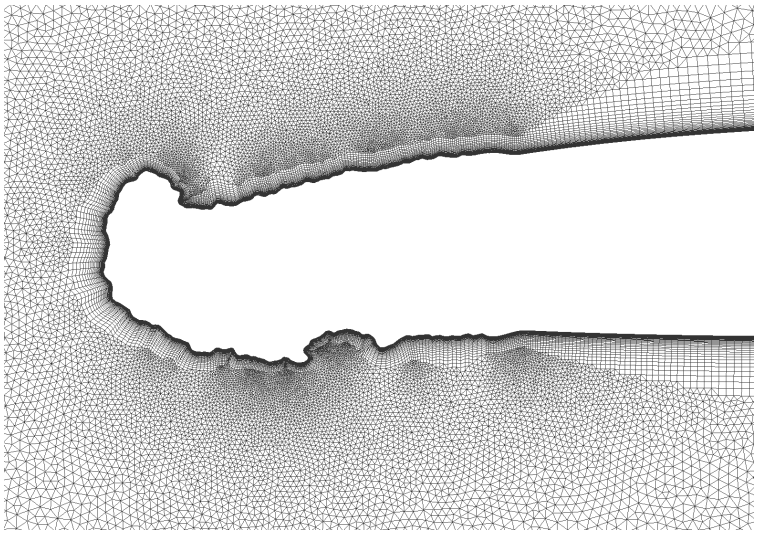

Fig. 3 Details of the grid with leading-edge ice.

III. Results

A. Validation

To validate the clean performance of the Fluent simulations, the lift and pitching moment coefficients for different control surface deflections are compared to the results of the panel code method of XFOIL, using an Ncrit of 9 [22]. Figures 4 and 5 compare the lift and moment coefficients for all five investigated deflection angles. In general, a good agreement is observed between the two methods. However, xFloil predicts a higher lift in all cases, especially close to the stall angle. The stall angle itself matches well between the two numerical methods. A significant outlier is the Fluent simulation with a control surface deflection of 15°, where a notable jump is observed at small AOAs.

The differences between Fluent and XFOIL can be explained by examining the differences in the curves of the pressure coefficients c_p. Figure 6 and 7 depict exemplarily a comparison between the c_p curves of Fluent and XFOIL for 0° and 15° surface deflection, respectively, at 0° AOA. For the 0° deflection angle case, a slightly reduced suction peak and a ca. 5% earlier transition are observed in the Fluent simulation, but are otherwise in good agreement. The earlier transition is likely an effect of the two different numerical methods used by Fluent and XFOIL to calculate the laminar-turbulent transition. In contrast, the 15° deflection angle case significantly differs between Fluent and XFOIL,

exhibiting considerably higher pressures on the suction side and no observable effect of the control surface deflection, suggesting a detached airflow in that area. The comparison of the moment coefficients shows a good agreement between Fluent and XFOIL for both the gradient of the curve and the magnitude.

The accreted ice on the leading edge is expected to produce laminar flow separations, especially for the horn ice shapes of the glaze ice shape. The size of the laminar separation bubble is expected to increase with the AOA. Figure 8 depicts the flow field of four different gaze ice cases: 0° and 4° AOA, and 0° and 15° control surface deflection. The effect of the increased size of the separation bubble can be confirmed. It is furthermore observable that the separation bubble increases in size with the deflection of the control surface.

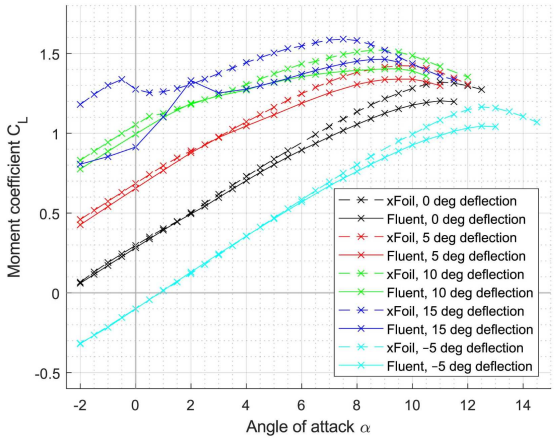

Fig. 4 Clean lift coefficient C_L for Fluent and XFOIL.

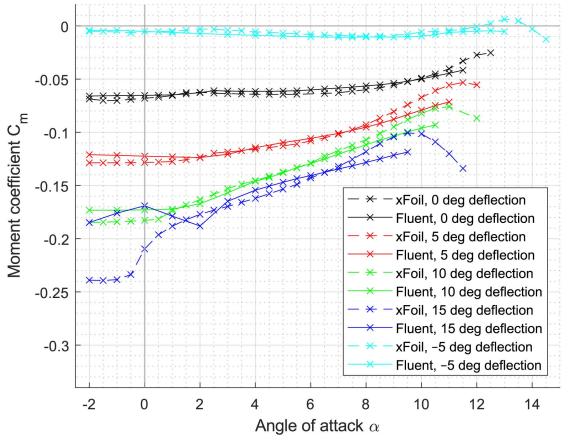

Fig. 5 Clean moement coefficient C_m for Fluent and XFOIL.

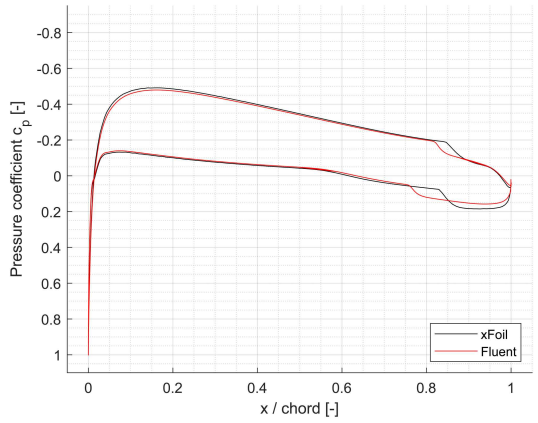

Fig. 6 Pressure coefficient c_p for 0° control surface deflection and 0° angle of attack.

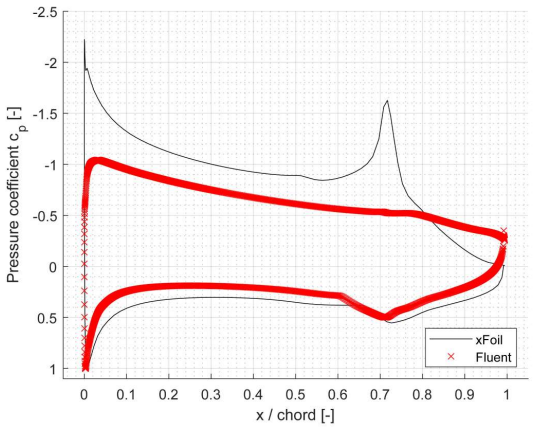

Fig. 7 Pressure coefficient c_p for 0° control surface deflection and 0° angle of attack.

(a) 0° AOA, 0° control surface deflection

(b) 4° AOA, 0° control surface deflection

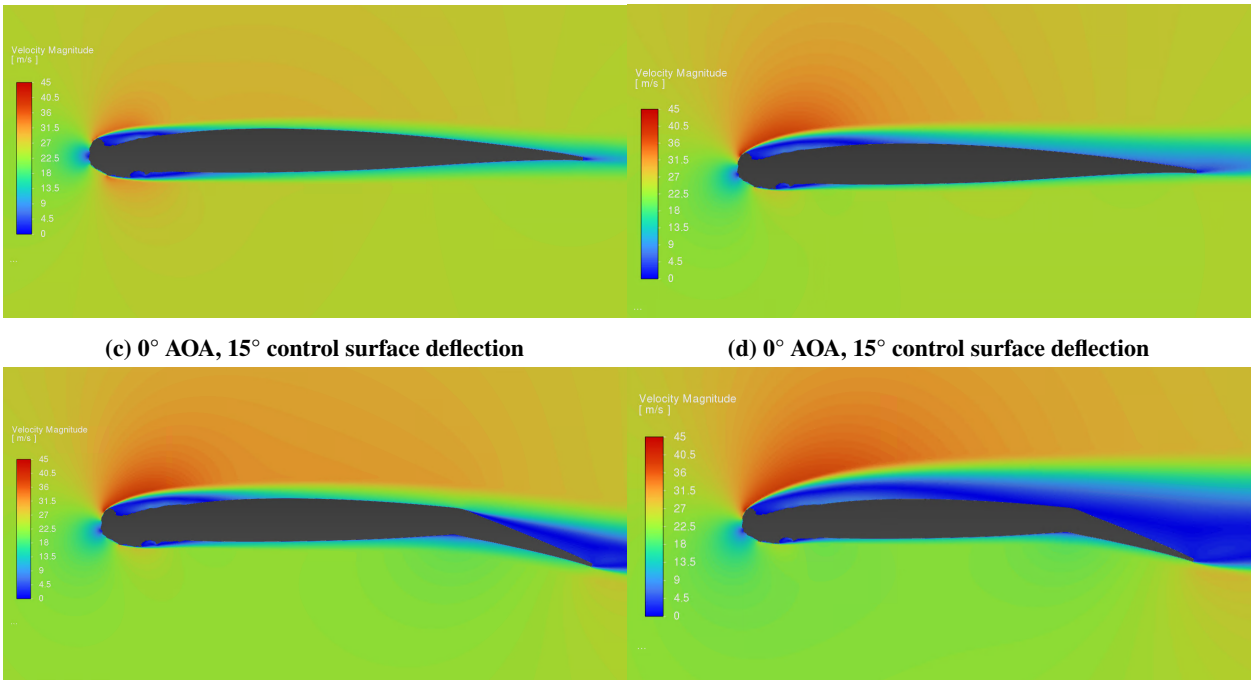

(c) 0° AOA, 15° control surface deflection

(d) 0° AOA, 15° control surface deflection

Fig. 8 Flow field around the glaze ice shape for two angles of attack and two control surface deflections.

B. Lift coefficient

In-flight icing has a significant impact on the lift. In [9], the performance degradation for airfoils without control surface deflection with numerically created ice shapes has been widely studied. In Fig 9, the performance degradation of the experimental MCCS ice shapes is depicted. A significant reduction in lift can be observed. The percentage decrease in maximum lift is 12%, 32%, and 45% for rime, mixed, and glaze, respectively.

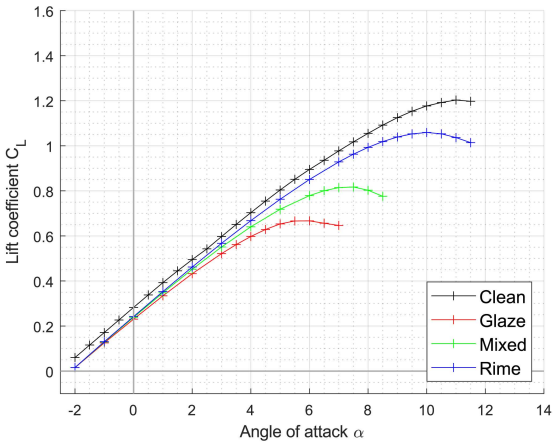

Fig. 9 Lift coefficient for 0° control surface deflection.

Following, the effect of the three ice types for different control surface deflections is evaluated. In Fig. 10, the lift polars of the various ice types are shown for the four different deflection angles. As expected, a significant reduction in stall angle is observed, with glaze being the most severe condition. Across all deflection angles, glaze reduces the stall

angle between 40% and 67% compared to the corresponding clean case, while the decrease is between 32% and 44% for mixed and between 5% and 11% for rime ice.

In the linear region of the lift polar, the degradation of the lift depends on the deflection angle. The degradation is evaluated here for 2° AOA instead of 4°, which is the usual flight AOA. The reason for that is that in some cases, this angle already experiences stall. Furthermore, the 15° control surface deflection case is excluded due to the atypical behaviour in that region. While only a marginal difference for the −5° deflection angle simulations is visually observable between iced and clean simulations, a constant offset is observed for all lift curves. It must be determined to what extent this offset is attributed to the different numerical methods used for turbulence. The magnitude of the offset increases with the deflection angle and has a more pronounced impact than the type of ice. At 0° deflection angle, the mean lift degradation is 9%, rising to 12%, 15%, and 19% for −5, 5°, and 10°, respectively. At 10° deflection angle, the effect of the individual ice shapes is most evident, increasing from 14% degradation for rime to 19% and 23% for mixed and glaze ice. A positive deflection of the control surface, in general, reduces the stall angle as can be observed in Fig. 4. In that case, especially for glaze ice, the onset of stall can be identified.

(a) Lift - −5° deflection

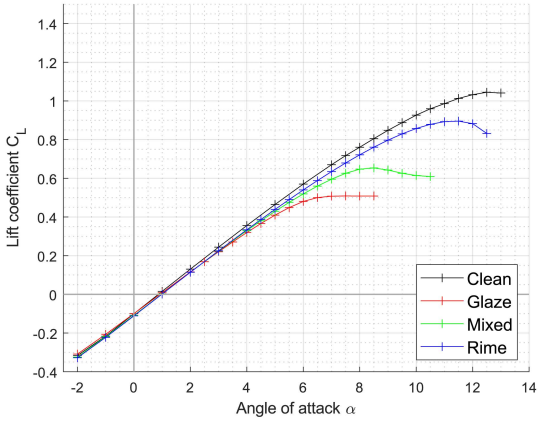

(b) Lift - 5° deflection

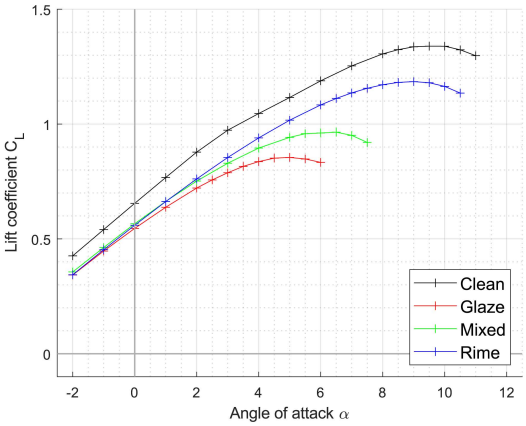

(c) Lift - 10° deflection

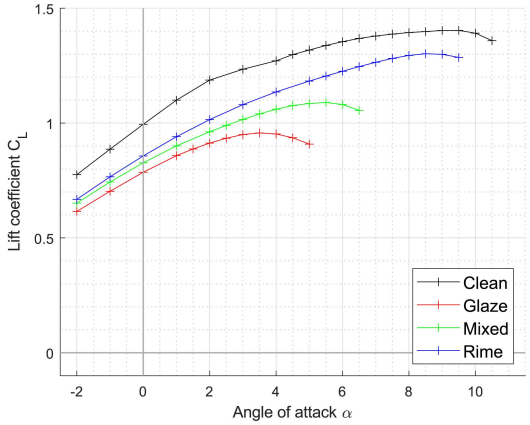

(d) Lift - 15° deflection

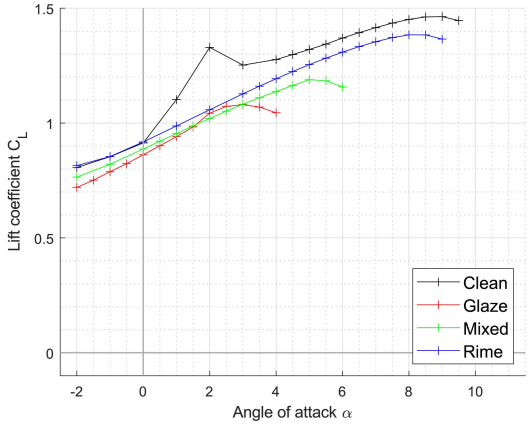

Fig. 10 Lift coefficient for different control surface deflection.

For a flight in unknown icing conditions, it is relevant to examine how lift changes for a specific ice shape for different deflections of the control surfaces. Fig. 11 depicts the lift polars for a wing with glaze ice accretion. During a (theoretical) level flight at a constant AOA of 5° - the increased AOA represents a counter-measure against the reduced lift compared to the clean airfoil - a deflection of the control surface by 5° already reaches $c_{L,max}$ due to the change lift curve, additional 5° deflection advance the flight condition beyond the stall angle with vibrations induced by instationary vortex sheedings [27]. The glaze ice shape is undoubtedly the most severe ice shape. However, it illustrates well the

mechanism involved when the control surface is deflected. The effect, analogous to glaze ice in Fig. 11, can be found for the clean case, and rime and mixed ice in Appendix B.

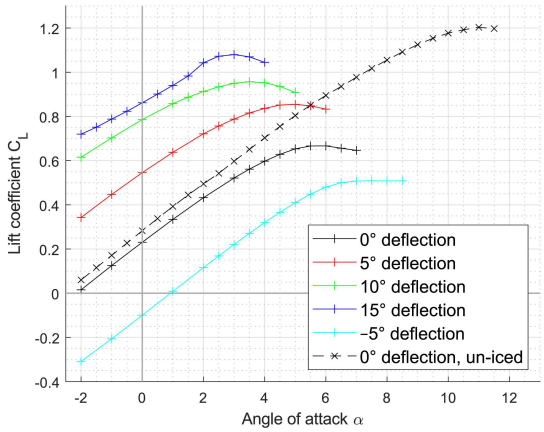

Fig. 11 Lift at different control surface deflection with glaze ice accumulation.

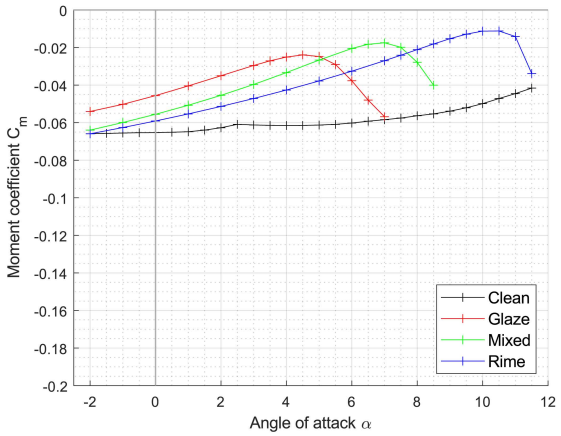

Fig. 12 Moment coefficient for 0° control surface deflection.

C. Pitching Moment

Figure 12 shows the curve of the pitching moment coefficient for clean and iced cases for 0° control surface deflection. To evaluate the longitudinal stability of an airfoil against disturbances, the gradient of the curve is significant. A negative gradient indicates a statically stable behaviour, meaning the airfoil creates a moment to return to the initial flight attitude after a disturbance. Consequently, a zero gradient indicates neutral static stability, while a positive gradient creates a moment that increases the disturbance. In the following figures, the scaling of the y-axis is kept identical to enable a better comparison between the individual plots.

The slope of the clean, un-iced configuration exhibits, over most of the AOA range, only a marginally positive slope, steepening as it approaches the stall angle. A small exception can be observed at 2.5° AOA, where a slight jump in the curve is noticeable. At about 8° AOA, the slope begins to become increasingly steeper. In contrast, all iced simulations feature a significantly greater positive gradient, revealing considerably more unstable behaviour.

This tendency is also observable in the simulations with control surface deflections. The clean cases feature significantly smaller slopes than the iced cases, with a −5° deflection exhibiting stable behavior over most of its AOA range. With increasing deflection angles, the initiation of more unstable behavior begins at lower AOAs, corresponding with the earlier onset of stall.

Analogous to the change in lift at different control surface deflections in Fig 11, the change of pitching moment for glaze ice is shown in Fig. 14. A positive deflection of the control surface reduces the moment coefficient, i.e., an additional nose-down moment is generated. The consequential decrease in angle of attack, generated by the positive slope of the curve for most of the AOA range, results in even more additional moments, leading to unstable behavior if no action is taken by the pilot or the autopilot. As for the lift coefficient, the change in pitching moment for the clean case, as well as for rime and mixed ice, can be found in Appendix B.

(a) Pitching Moment - −5° deflection

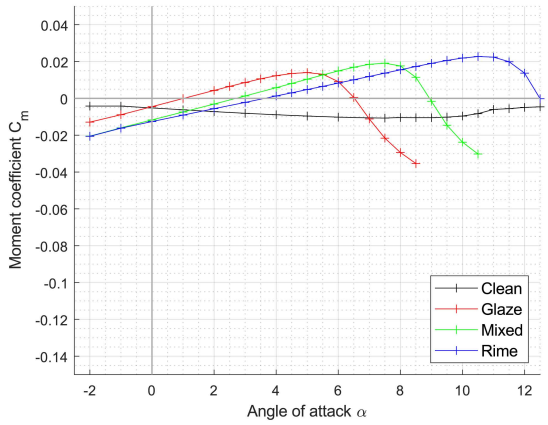

(b) Pitching Moment - 5° deflection

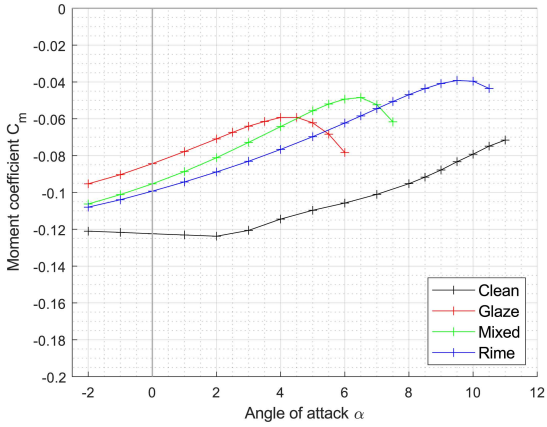

(c) Pitching Moment - 10° deflection

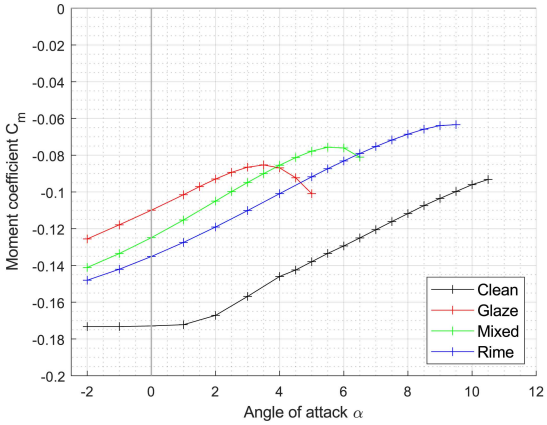

(d) Pitching Moment - 15° deflection

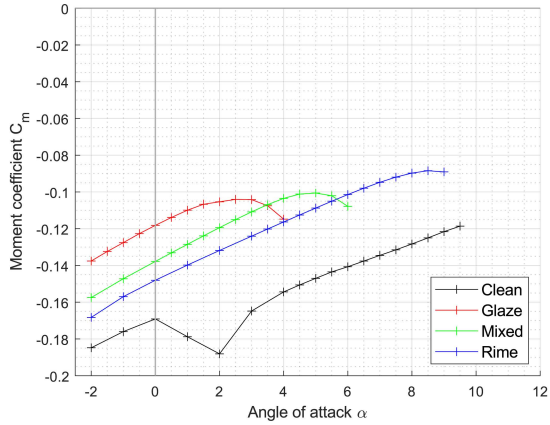

Fig. 13 Moment coefficient for different control surface deflection.

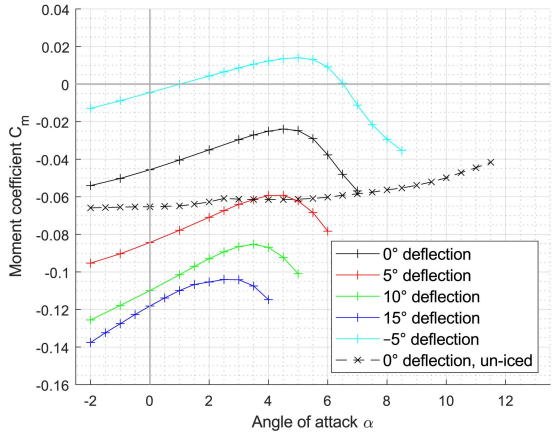

Fig. 14 Moment Coefficient at different control surface deflection with glaze ice accumulation.

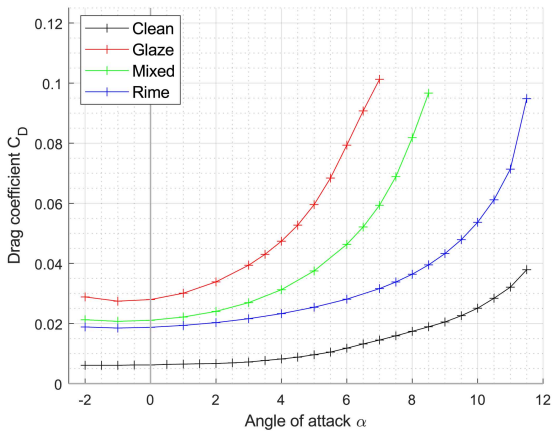

Fig. 15 Drag coefficient for the clean and iced undeflected airfoil.

D. Drag coefficient

Leading-edge ice accretion increases the drag of the airfoil. While the drag increase for an iced airfoil without control surface deflection can be significant, a deflection of the control surface increases this effect even more.

At the nominal flight AOA of 4°, the drag increases for 0° control surface deflection by 480%, 280%, and 180% for glaze, mixed, and rime ice, respectively. This is depicted in Fig. 15. Deflecting the control surface increases the drag even further, as can be seen in Fig 16. Independent of the ice shape, a deflection of the control surface by 5° increases the drag by 30-34%, for 10° 82-83%, and for 15° 146-156%, compared to the corresponding iced, 0° deflection case. One outlier is the 10°, rime ice case, where the increase is only 61%.

The worst performance degradation compared to the corresponding clean deflection case is observed for the glaze ice case. A drag increase of 450%, 440%, 330%, and 190% for −5°, 5°, 10°, and 15° deflection can be seen. However, the value for the 15° deflection case should be taken with caution, as discussed earlier.

(a) Drag - Clean Airfoil

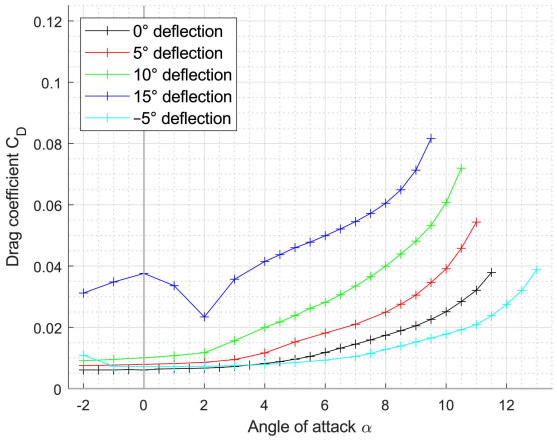

(b) Drag - Glaze Ice

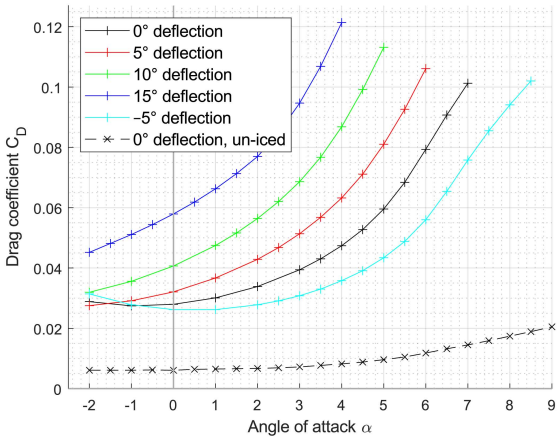

(c) Drag - Mixed Ice

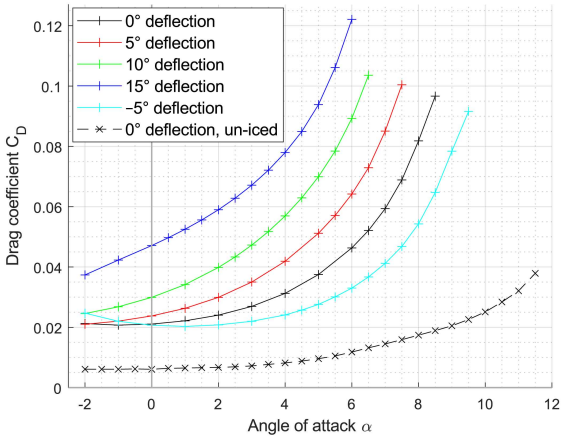

(d) Drag - Rime Ice

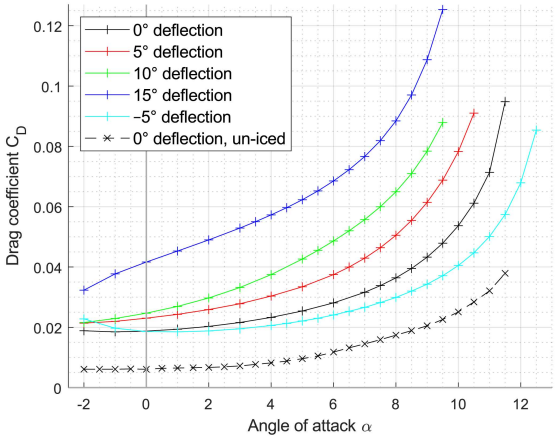

Fig. 16 Drag coefficient of the clear wing and for different ice shapes.

E. Stall speed

Leading-edge ice accretion has a significant influence on $C_{L,max}$. A comparison of the stall speed for a hypothetical UAV with a wing area of 0.85 m^2, a weight of 25 kg, and flying at 0 °C can be seen in Fig. 17. In these simplified calculations, possible 3D effects or additional lift from the fuselage or an empennage are neglected.

Depending on the control surface deflection angle and the type of ice, the minimal required velocity to maintain horizontal flight increases significantly compared to the clean airfoil. In the worst case, at −5° deflection, the stall speed

increases by 43%, 27%, and 8% for glaze, mixed, and rime, respectively. However, with increasing control surface deflection, the additional required velocity decreases.

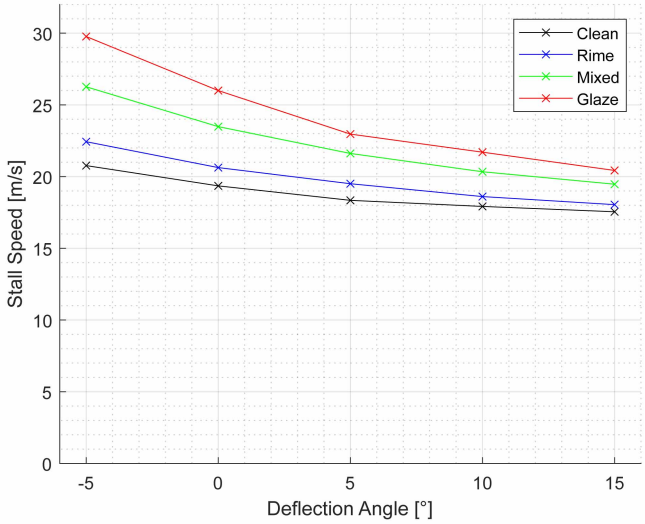

Fig. 17 Comparison of stall speeds for different control surface deflection angles and ice types.

F. Control derivatives

The results of the changed lift and moment coefficient in an iced state have implications for the performance and controllability of the UAV. The longitudinal control derivatives $C_{L_{\delta_e}}$ and $C_{m_{\delta_e}}$ are defined as the changes in lift and moment when deflecting the control surface. This can be used in a simulator to study the flight behavior of an iced UAV. The first attempts to model an iced UAV were made by Högnadottir et al. in [16], which include an aerodynamic model to describe the flight behavior. A more sophisticated model is presented in [28]. This is an example of an aerodynamic model where the effects of atmospheric icing can be incorporated by modifying the control derivatives, as presented in this publication.

To be consistent with the definitions of the control derivatives used in the simulators, the change of deflection angle in the calculation of the derivatives is defined in radians [29]. The evaluation of change in lift and moment is in comparison with the undeflected cases.

Figures 18 and 19 display the control derivatives $C_{L_{\delta_e}}$ and $C_{m_{\delta_e}}$ for the clean wing and with leading-edge ice accretion of three ice types for the flight AOA of 4°. Additional figures for 0° AOA are presented in Appendix C. Compared to the clean wing, all iced cases produce less additional lift, making the control surfaces less effective. The worst condition is glaze ice with a mean decrease in effectiveness of 27%, followed by mixed ice with 19%, and rime ice with 13%. Furthermore, in the iced cases less pitching moment is produced. The percentage change compared to the clean case at 4° AOA is depicted in Table 3.

Table 3 Relative change of the control derivatives for different ice shapes and control surface deflections at 4° AOA.

	$C_{L_{\delta_e}}$				$C_{m_{\delta_e}}$			
	−5°	5°	10°	15°	−5°	5°	10°	15°
Rime	−3.9%	−20.6%	−17.6%	−8.4%	−16.5%	−35.8%	−31.0%	−20.7%
Mixed	−10.5%	−25.5%	−26.1%	−13.4%	−25.6%	−41.7%	−38.3%	−24.5%
Glaze	−20.0%	−30.3%	−37.5%	−22.2%	−29.0%	−35.4%	−26.8%	−3.3%

To gain a broader understanding of the range validity of these control derivatives, their dependency on flight velocity is illustrated in Figs. 20 and 21 for the entire operational range of a UAV with the dimensions mentioned in Chapter III.E.

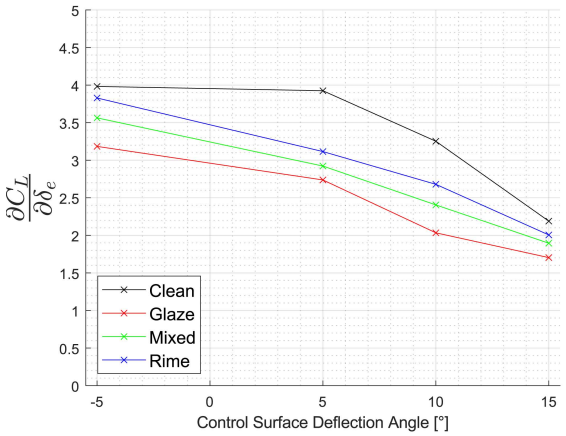

Fig. 18 Change of $C_{L_{\delta_e}}$ in iced conditions at 4° angle of attack.

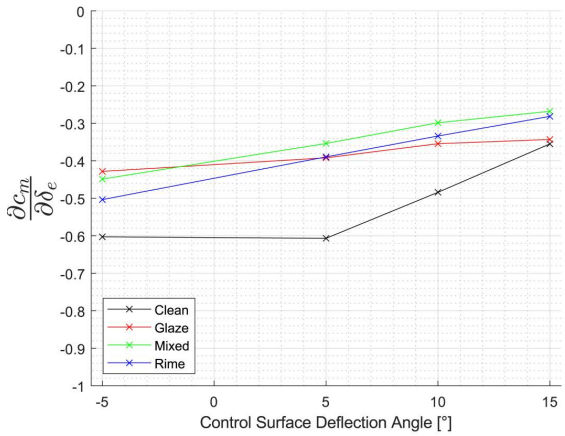

Fig. 19 Change of $C_{m_{\delta_e}}$ in iced conditions at 4° angle of attack.

The chosen control surface deflection for this study is 5°. For both, $C_{L_{\delta_e}}$ and $C_{m_{\delta_e}}$, no significant dependency on the velocity can be found. This is in contrast to the results published in [17]. However, the investigated range of velocity in that publication was substantially higher and wider.

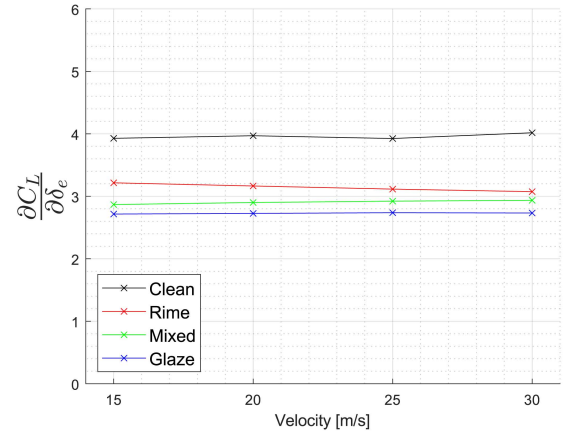

Fig. 20 Velocity dependency of $C_{L_{\delta_e}}$ in iced conditions at 4° angle of attack.

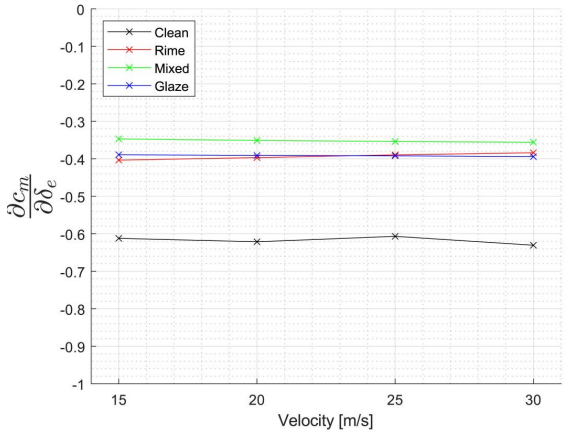

Fig. 21 Velocity dependency of $C_{m_{\delta_e}}$ in iced conditions at 4° angle of attack.

IV. Discussion

The purpose of this study was to investigate the influence of leading-edge ice accretion on the control surfaces. Performing CFD simulations on iced geometries reveals limitations of CFD simulations, which are widely discussed in [30]. The evaluated parameters are the lift and moment coefficients, from which the coefficients $C_{L_{\delta_e}}$ and $C_{m_{\delta_e}}$ are derived. The results were generated using CFD simulations in 2D and steady state. This poses the disadvantage that some effects, like the influence of the wing tip vortex, might not have been captured. Other effects, like a sweep angle of the wing, can be neglected [31]. Performing simulations steady state is computationally cheaper, but overlooks transient phenomena. Ice shapes like the presented glaze ice shape horns, especially on the suction side. These produce laminar separation bubbles, whose extent has a transient character [27]. Investigated cases with high deflection angles of the control surface revealed that the airflow was unable to follow the sudden change in geometry, likely resulting in oscillating flows.

Simulations with high deflection angles, such as the clean 15° deflection angle simulation, exhibited unexpected effects, as evident between 0° and 3° AOA. The reason for the sudden increase and decrease in lift needs to be determined. Trial simulations, which were run fully turbulent, do not exhibit this behavior in the lift curve. It is therefore likely that this effect can be attributed to the transition from laminar to turbulent flow.

The simulations of the clean airfoil were conducted using a turbulence model with transition and a smooth wing geometry. In contrast, the simulations with ice shapes were run fully turbulent and with roughness at the location of the ice. The effects of these two approaches on lift, drag, and pitching moment require further investigation, which exceeds the scope of this work. The influence of the roughness is depicted in Appendix A and shows little impact of the roughness height except for a deflection on the control surface. Additionally, this effect requires further research.

The stall speed discussed in Chapter III.E suggests that the velocity, depending on the deflection angle, needs to be increased to maintain level flight when ice accretion is present. The increased velocity produces more drag that needs to be overcome by thrust from the propeller. Especially in the case of glaze ice and $-5°$ deflection angle, the propeller might not be able to provide the required thrust.

While this paper investigates experimental ice shapes accumulated for 20 minutes, it is unlikely that in real-life conditions, a UAV will accrete that much ice before escaping the cloud or crashing. Ice accretion is a continuous process, and the aerodynamic performance degradation increases with time. Therefore, generating time-resolved ice shapes that represent various stages of accretion and their effects on aerodynamics, with or without control surface deflection, would be beneficial for understanding the complete process.

Employing ice protection systems to mitigate ice accretion will significantly improve the performance of the UAV. However, most ice protection systems are operated in de-icing mode and will allow little ice to build up. This already impairs the aerodynamic performance [32]. Building on those results, the influence on the control surfaces also needs further investigation.

V. Conclusion

This paper compared the effect of leading-edge ice accretion on a control surface using 2D CFD simulations. The basis of the study are three ice shapes that were accumulated in an icing wind tunnel experiment, representing glaze, mixed, and rime ice. The ice shapes were accreted for 20 minutes and represent a flight through a CFR 14 Part 25 Appendix C continuous maximum cloud. Their influence on the lift and pitching moment coefficient has been investigated for five control surface deflections, $-5°$, $0°$, $5°$, $10°$, and $15°$. Furthermore, the influence on stall speed and control derivatives was evaluated.

All ice shapes result in a reduction in lift and stall angle, with glaze ice being the most severe ice type. A deflection of the control surface in a positive direction results in additional lift, although it is less than in the clean case. Depending on the ice shape and surface deflection, the stall angle is significantly reduced, and it can occur in a worst-case scenario of glaze ice and 15° deflection as early as 3°. The curve of the pitching moment coefficient experiences a steeper positive gradient compared to the clean case. This can lead to unstable behavior and a nose-down moment when the control surface is deflected. Due to the reduced $C_{L,max}$, the stall speed increases considerably. The required additional velocity to enable a stable horizontal flight produces additional drag, which the propeller might not be able to compensate for. The longitudinal control derivatives $C_{L_{\delta_e}}$ and $C_{m_{\delta_e}}$ exhibit reduced control surface effectiveness due to leading-edge ice accretion. However, a dependency of the control derivatives on the flight velocity could not be found.

The investigated ice shapes and thus the results represent the effects of 20 minutes of ice accretion. Time-resolved ice shapes ice shapes for 5, 10, and 15 minutes would provide a more comprehensive perspective.

Appendix

A. Comparison of different equivalent sand-grain ice roughness heights

Depicted in Appendix A are the lift curves for three equivalent sand-grain-roughness heights: the roughness heights used in this publication, double the height, and no roughness. Furthermore, Figs. 22 and 23 show the lift curves with the used roughness, but, in contrast to the other iced simulations, which were calculated fully turbulent, these are calculated with transition. The cases investigated in this short study are 0° control surface deflection for rime and glaze ice, and 5° deflection for rime ice. Figure 22 and 23 show very good agreement between the different simulation settings. Only in the stall area are slight differences visible for the transitional case. However, for the rime case with 5° deflection, a significant offset is perceivable.

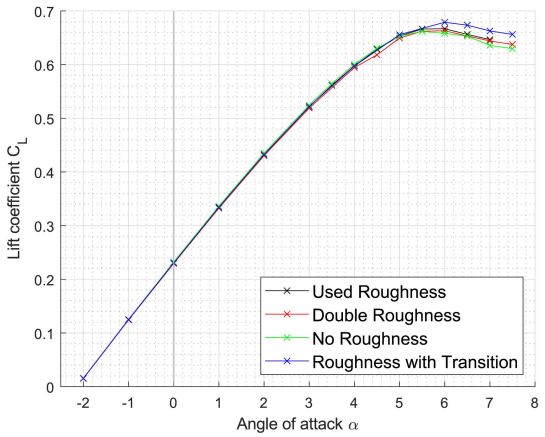

Fig. 22 Comparison of different glaze ice roughness heights and transition, 0° deflection.

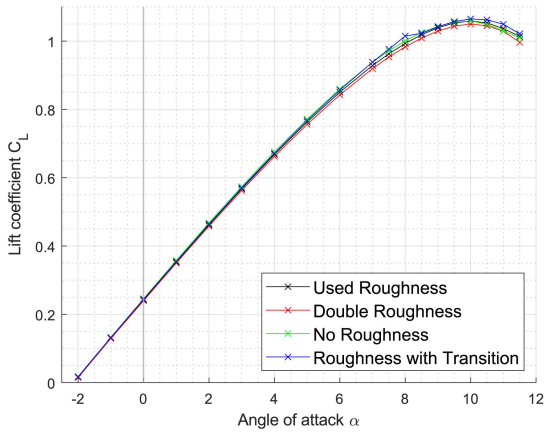

Fig. 23 Comparison of different rime ice roughness heights and transition, 0° deflection.

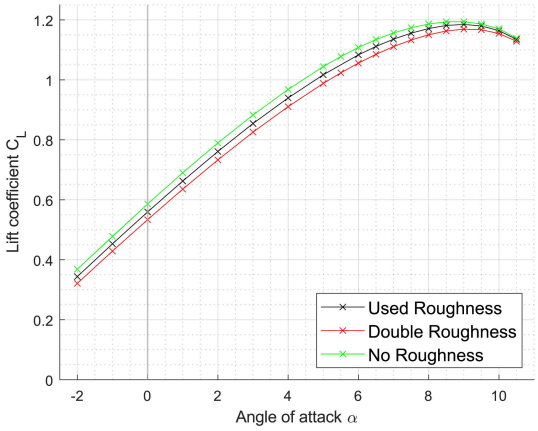

Fig. 24 Comparison of different rime ice roughness heights, 5° deflection.

B. Additional Lift and Pitching Moment Plots

(a) Lift Coefficient **(b) Pitching Moment Coefficient**

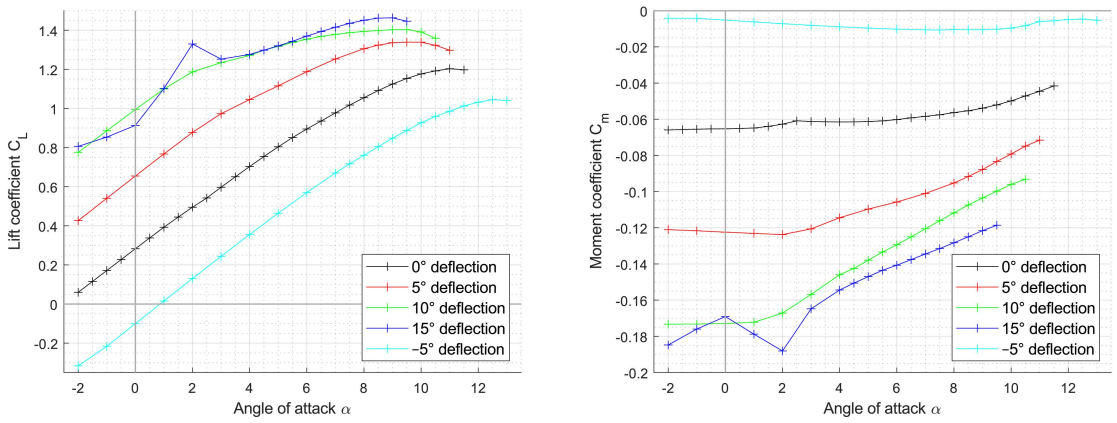

Fig. 25 Additional plots for the clean airfoil.

(a) Lift Coefficient **(b) Pitching Moment Coefficient**

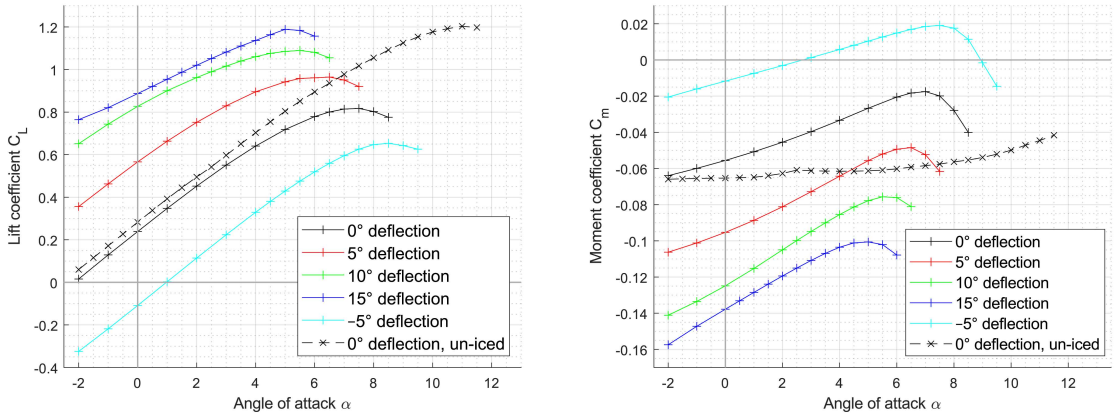

Fig. 26 Additional plots for mixed ice.

(a) Lift Coefficient **(b) Pitching Moment Coefficient**

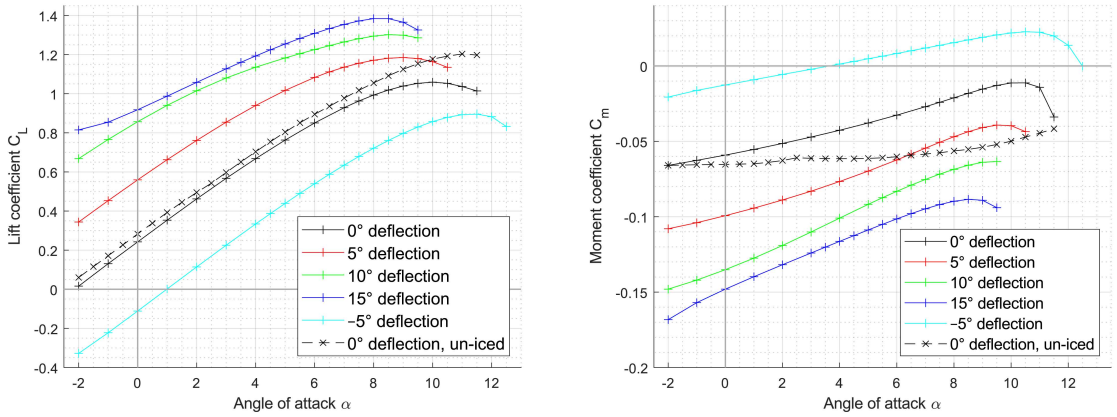

Fig. 27 Additional plots for rime ice.

C. Control Derivatives at 0° Angle of Attack

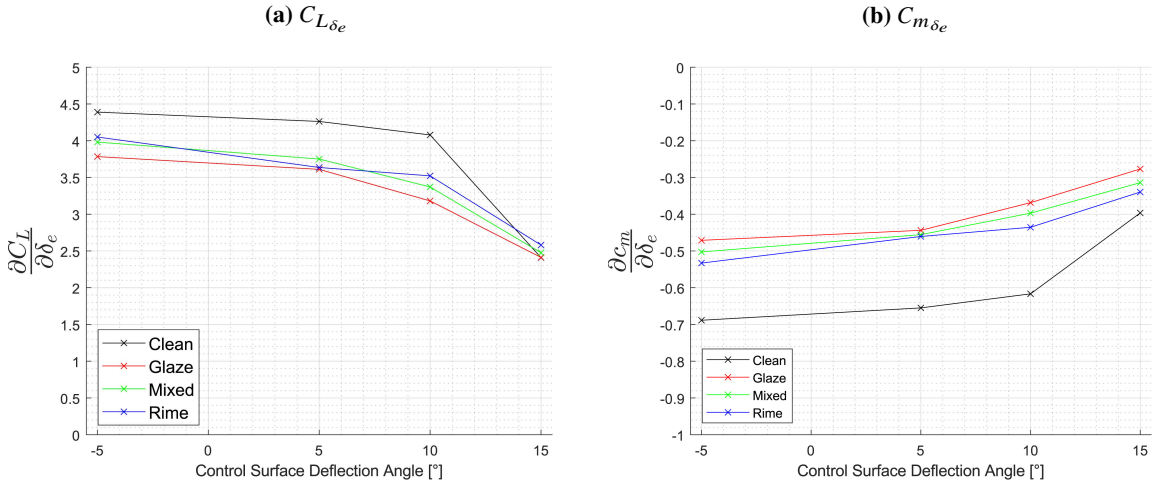

Fig. 28 Control derivatives for 0° AOA

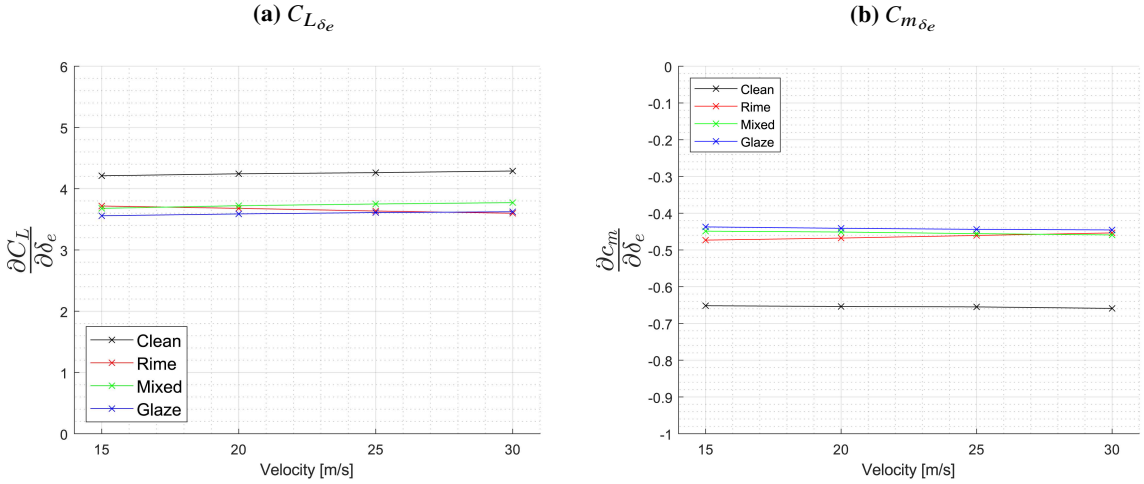

Fig. 29 Velocity dependency for 0° angle of attack.

Table 4 Relative change of the control derivatives for different ice shapes and control surface deflections at 0° AOA.

	$C_{L_{\delta_e}}$				$C_{m_{\delta_e}}$			
	−5°	5°	10°	15°	−5°	5°	10°	15°
Rime	−7.7%	−14.7%	−13.6%	7.1%	−22.6%	−29.7%	−29.4%	−14.3%
Mixed	−9.3%	−12.0%	−17.3%	2.8%	−27.0%	−30.4%	−35.6%	−20.8%
Glaze	−13.8%	−15.3%	−22.0%	0.1%	−31.6%	−32.2%	−40.2%	−30.2%

Acknowledgments

The work is partly sponsored by the Research Council of Norway through project 316425. The numerical simulations were performed on resources provided by the National Infrastructure for High-Performance Computing and Data Storage in Norway (UNINETT Sigma2) on the Fram supercomputer, under project code NN9613K Notur/NorStore.

References

[1] Hann, R., and Johansen, T. A., "Unsettled Topics in Unmanned Aerial Vehicle Icing," *SAE Research Report EPR2020008*, 2020. https://doi.org/10.4271/EPR2020008.

[2] Federal Aviation Administration, "Part I — Atmospheric Icing Conditions," *CFR 14 Part 25 Appendix C*, 2016.

[3] Federal Aviation Administration, "Appendix O to Part 25 — Supercooled Large Drop Icing Conditions," *CFR 14 Part 25 Appendix O*, 2016.

[4] Anderson, D. N., and Tsao, J.-C., "Evaluation and Validation of the Messinger Freezing Fraction," *41st Aerospace Sciences Meeting and Exhibit*, AIAA, 2003. https://doi.org/10.2514/6.2003-1218, URL http://www.sti.nasa.gov.

[5] Janjua, Z. A., Turnbull, B., Hibberd, S., and Choi, K. S., "Mixed ice accretion on aircraft wings," *Physics of Fluids*, Vol. 30, No. 2, 2018. https://doi.org/10.1063/1.5007301.

[6] Bragg, M. B., Broeren, A. P., and Blumenthal, L. A., "Iced-airfoil aerodynamics," , 2005. https://doi.org/10.1016/j.paerosci.2005.07.001.

[7] Cao, Y., Tan, W., and Wu, Z., "Aircraft icing: An ongoing threat to aviation safety," , 4 2018. https://doi.org/10.1016/j.ast.2017.12.028.

[8] Jäckel, R., Gutiérrez-Urueta, G., and Tapia, F., "A review on Pitot tube icing in aeronautics: Research- design and characterization – future trends," *Flow Measurement and Instrumentation*, Vol. 81, 2021, p. 102033. https://doi.org/https://doi.org/10.1016/j.flowmeasinst.2021.102033, URL https://www.sciencedirect.com/science/article/pii/S0955598621001394.

[9] Lindner, M., Wallisch, J., and Hann, R., "UAV Icing: Numerical Simulation of Icing Effects on Wing and Empennage," *SAE Technical Paper 2023-01-1384*, 2023. https://doi.org/10.4271/2023-01-1384, URL https://www.sae.org/content/2023-01-1384.

[10] Müller, N. C., Løw-Hansen, B., Borup, K. T., and Hann, R., "UAV icing: Development of an ice protection system for the propeller of a small UAV," *Cold Regions Science and Technology*, Vol. 213, 2023, p. 103938. https://doi.org/10.1016/j.coldregions.2023.103938, URL https://linkinghub.elsevier.com/retrieve/pii/S0165232X23001684.

[11] Müller, N. C., and Hann, R., "UAV Icing: 3D Simulations of Propeller Icing Effects and Anti-Icing Heat Loads," *International Conference on Icing of Aircraft, Engines, and Structures*, SAE International, 2023. https://doi.org/https://doi.org/10.4271/2023-01-1383, URL https://doi.org/10.4271/2023-01-1383.

[12] Broeren, A. P., Addy, H. E., and Bragg, M. B., "Flowfield Measurements about an Airfoil with Leading-Edge Ice Shapes," *Journal of Aircraft*, Vol. 43, No. 4, 2004. https://doi.org/10.2514/1.19021.

[13] Muhammed, M., and Virk, M. S., "On the Fidelity of RANS-Based Turbulence Models in Modeling the Laminar Separation Bubble and Ice-Induced Separation Bubble at Low Reynolds Numbers on Unmanned Aerial Vehicle Airfoil," *Drones*, Vol. 8, No. 4, 2024. https://doi.org/10.3390/drones8040148.

[14] Oo, N. L., Richards, P. J., and Sharma, R. N., "Ice-induced separation bubble on RG-15 airfoil at low reynolds number," *AIAA Journal*, Vol. 58, No. 12, 2020, pp. 5156–5167. https://doi.org/10.2514/1.J059257.

[15] Ratvasky, T. P., VanZante, J. F., and Sim, A., "NASA/FAA Tailplane Icing Program: Flight Test Report," Tech. rep., NASA Glenn Research Center, 2000.

[16] Högnadottir, S., Gryte, K., Hann, R., and Johansen, T. A., "Inner-Loop Control of Fixed-Wing Unmanned Aerial Vehicles in Icing Conditions," *AIAA SCITECH 2023 Forum*, 2023. https://doi.org/10.2514/6.2023-1049.

[17] Ranaudo, R., Reehorst, A., Bond, T., Batterson, J., and O'Mara, T., "Determination of longitudinal aerodynamic derivatives using flight data from an icing research aircraft," American Institute of Aeronautics and Astronautics (AIAA), 1989. https://doi.org/10.2514/6.1989-754.

[18] Baars, W. J., Stearman, R. O., and Tinney, C. E., "A Review on the Impact of Icing on Aircraft Stability and Control," Vol. 2, No. 1, 2010, pp. 35–52. https://doi.org/10.3293/asdj.2010.7, URL http://www.cessna.com/caravan/grand-.

[19] Tiihonen, M., Jokela, T., Makkonen, L., and Bluemink, G.-J., "VTT Icing wind tunnel 2.0," *In Proceedings of the Winterwind*, 2016.

[20] Hann, R., Müller, N., Lindner, M., and Wallisch, J., "UAV Icing: Experimental Validation Data for Predicting ice Shapes at Low Reynolds Numbers," *SAE Technical Papers*, SAE International, 2023. https://doi.org/10.4271/2023-01-1372.

[21] Henzler, M., "CFD-Simulation of Icing on a Flying-Wing UAV," Master's thesis, University of Stuttgart, NTNU, 2024.

[22] Drela, M., "XFOIL: An Analysis and Design System for Low Reynolds Number Airfoils," *Low Reynolds Number Aerodynamics*, edited by T. J. Mueller, Springer Berlin Heidelberg, Berlin, Heidelberg, 1989, pp. 1–12.

[23] Ansys Inc., *Ansys Fluent User's Guide - Release 2025 R1*, 2025.

[24] Ansys Inc., *Ansys Fluent Theory Guide - Release 2025 R1*, 2025.

[25] Shin, J., Berkowitz, B., Chen, H. H., and Cebeci, T., "Prediction of ice shapes and their effect on airfoil drag," *Journal of Aircraft*, Vol. 31, No. 2, 1994, pp. 263–270. https://doi.org/10.2514/3.46483.

[26] Cadence Design Systems, Inc., *Pointwise User Manual*, 2024. Available at https://www.cadence.com/doc/user-manual/, accessed on 20.11.2024.

[27] Ansell, P. J., and Bragg, M. B., "Unsteady modes in flowfield about airfoil with horn-ice shape," *Journal of Aircraft*, Vol. 53, American Institute of Aeronautics and Astronautics Inc., 2016, pp. 475–486. https://doi.org/10.2514/1.C033421.

[28] Løw-Hansen, B., Hann, R., Gryte, K., Johansen, T. A., and Deiler, C., "Modeling and identification of a small fixed-wing UAV using estimated aerodynamic angles," *CEAS Aeronautical Journal*, Vol. 16, 2025, pp. 501–523. https://doi.org/10.1007/s13272-025-00816-3, URL https://doi.org/10.1007/s13272-025-00816-3.

[29] Klein, V., and Morelli, E. A., *Aircraft System Identification - Theory and Practice*, American Institute of Aeronautics and Astronautics, Inc., 2006.

[30] Hann, R., *Numerical Simulation of In-Flight Icing of Unmanned Aerial Vehicles*, Springer International Publishing, Cham, 2020, pp. 1–44. https://doi.org/10.1007/978-3-030-64725-4_12-1, URL https://doi.org/10.1007/978-3-030-64725-4_12-1.

[31] Lindner, M., and Hann, R., "UAV Icing: Comparison of Simulated 3D and 2D Ice Accretion on Wings," *AIAA Aviation Forum and Ascend 2024*, AIAA, Las Vegas, 2024. https://doi.org/https://doi.org/10.2514/6.2024-4451.

[32] Wallisch, J., Lindner, M., Petersen, O. W., Neunaber, I., Bracchi, T., Hearst, R. J., and Hann, R., "UAV Icing: Aerodynamic Degradation Caused by Intercycle and Runback Ice Shapes on an RG-15 Airfoil," *Drones*, Vol. 8, No. 12, 2024. https://doi.org/10.3390/drones8120775.